SILAR deposition and characterization of ZnO films for numerical investigation as electron transport layer in solar cells

P. Sreedev[a,b], V. Rakhesh[b,*]
[a]*Research and Development Centre, Bharathiar University, Coimbatore, India – 641 046*
[b]*Department of Physics, Amrita School of Physical Sciences, Amrita Vishwa Vidyapeetham, Amritapuri, India -690525*

The SILAR method of thin film deposition has attracted the scientific community over the years due to its easiness, low cost, availability of room temperature deposition, and more over due to the variation in properties of thin films available by varying deposition parameters.This work is carried out in a way to comprehensively compare two ZnO thin film samples prepared from precursor media with Zinc Acetate (S1) and Zinc Chloride(S2) salts deposited by SILAR method in Perovskite Solar cell applications. The XRD, FTIR, Raman, FESEM, and UV-Visible analysis were carried out for identifying the structural, morphological, and optical quality of these samples. The role of these samples as Electron Transport Layer (ETL) in Perovskite Solar cell were identified using General purpose PhotoVoltaic Device model (GPVDM) simulation software which is well adapted for studying Solar cell architecture. It provided the output Solar cell parameters like J_{sc}, V_{oc}, FF, PCE, etc and by varying the active layer and Hole Transport Layer (HTL) thicknesses, the optimized efficiency of devices with samples S1 and S2 were obtained as 21.88% and 21.96%.The results showed that SILAR-synthesized ZnO thin films could be potential candidates for ETL applications in Perovskite Solar cells.

(Received May 20, 2024; Accepted August 8, 2024)

Keywords: ZnO thin films, SILAR method, XRD, FESEM, FTIR, Raman spectra, UV-visible studies, GPVDM, Solar cell

1. Introduction

ZnO in the form of thin films findsa wide variety of applications in optoelectronic devices like Solar cells, Field Effect Transistors, transparent windows, sensors, etc owing to its unique property that it could be manifested in different nano morphologies like nanorods, nanoflowers, nano spherical granules, etc[1 − 5]. The selectionof nano thin film in optoelectronic applications depends on its crystalline structure with loosely bounded bonds, high surface-to-volume ratio, high porosity, and good electrical properties which all will enhance charge mobility through the thin film[6 − 9]. Nano ZnO thin films act as transparent conducting films in most optoelectronic applications, ultimately helping in the miniaturization of devices. The synthesis of ZnO films for this applications are possible by simple chemical solution methods like Sucsessive Ion Layer Adsorption and Reaction (SILAR) [10 − 12] . SILAR is a cost-effective, easily achievable method,which utilizes chemical techniques at room temperature for the synthesis of thin films and is suitable over a wide variety of substrates.In low-energy device fabrication, the consumer cost could be minimized to a considerable amount with this method. Moreover, the tailoring of nano morphology and property of thin films could be possible by an appropriate selection of precursors and reaction conditions.[13 − 16].

Perovskite Solar cells have attracted the attention of the scientific community over the years, due to the advantages like flexibility, lightweight, easy processing methods, low cost, and mainly due to the high efficiency available compared to other thin film Solar cells[17 − 21]. By increasing light absorption in the active layer, the efficiency of these Solar cells could be improved. Moreover,

* Corresponding author: rakheshv@am.amrita.edu
https://doi.org/10.15251/JOR.2024.204.551

if maximum photons are converted to electric charges and if those are efficiently extracted to electrodes, the performance of the Solar cell could be improved to further extend [22 – 25]. The Electron Transport Layer (ETL) and Hole Transport Layer (HTL) are fixed on either side of the active layer so that the desired charges without recombination only reach to cathode and anode respectively. Transparent conducting oxides (TCO), which are optically transparent and electrically conductive are preferred as ETL in Solar cells. N-type semiconducting materials like Zinc oxide (ZnO) are ideal for this purpose in providing a low resistive path for electrons to the cathode and also in blocking the holes [26 – 30]. ZnO thin films are having advantages like high transparency in the visible range with optical band gap around 3.37eV , the excitonic binding energy of 60meV with good electron mobility, availability of simple deposition methods, and also chemically non-toxic nature[31 – 33]. The theoretical prediction of its performance in Solar cells is possible with simulation software like General Purpose PhotoVoltaic Device Model (GPVDM) [34 – 35]. For both electrons and holes, GPVDM resolves the continuity, drift-diffusion, and Poisson's equations. The finite difference method is used to solve the drift-diffusion equations in coordinate space for identifying the charge flow inside the device.

The present work has been carried out in studying the comparative analysis of ZnO nanostructured thin films synthesized by the SILAR method from two different precursor media for Perovskite Solar cell applications. Both experimental and numerical methodologies have been made used in this study. From Zinc Acetate and Zinc Chloride salts, precursor solutions were prepared, and using the SILAR method, ZnO thin films were deposited on glass substrates.After completing their structural, morphological, and optical investigations, parameters are extracted for the simulation of Perovskite Solar cells using GPVDM. From the numerically fabricated Solar cell, parameters like J_{sc}, V_{oc}, FF, PCE, etc are identified by obtaining current density-voltage(J-V) measurement.Fabrication of ZnO-basedPerovskite Solar cells is important for economical viability, better performance, and stability enhancement, as it will drastically trim the cost of production and also will increase efficiency. The objective of the current work is to compare ZnO thin films obtained from two different precursor media in fabricating stable, cost-effective, and highly efficient Perovskite Solar cell devices.

2. Experimental

2.1. Deposition of thin films

Thin films were synthesized by the SILAR method using automated temperature-controlled SILAR equipment. Here two different precursors of 0.1M concentration were utilized as cationic solutions with Zinc Acetate and Zinc Chloride. The corresponding anionic solution was deionized water. Two different cationic solutions were prepared by mixing the respective Zinc salt with distilled water. The PH of the obtained precursors was maintained at 9 by adding ammonia buffer solution. The distilled water is kept as anioanic solution, maintained at 80^0C, which is the optimum condition for the reaction to take place in SILAR. The cationic chemicals and Ammonia buffer solution were provided by Merk India(Pvt.ltd).

Deposition of ZnO thin films was carried out on corning glass substrates. Initially, the substrates were immersed in dilute HNO_3 and were cleaned many times with running water and distilled water. Thus obtained substrates were further cleansed with acetone before the coating procedure. Prepared substrates underwent 50 SILAR dip cycles alternately in cationic and anionic solutions. After deposition, samples were dried in air and then annealed at 450^0C for 1 hour. Thus obtained ZnO thin film samples from Zinc acetate and Zinc chloride precursors were labeled as samples S1 and sample S2 respectively[36 – 37]. The Scematic idea of ZnO film deposition is presented in Figure 1.

2.2. Characterization

X-ray diffraction spectra of the prepared samples were recorded using an X-ray diffractometer(Bruker AXS D8 Advance) with k_α wave length $1.54056A^0$. Scanning Electron Microscopy (JEOL Model JSM - 6390LV) was employed in analyzing the surface morphology of the samples. Electrical conductivity measurements were carried out by four probe method using

Keithley 2400 source meter. Optical transmittance data of the samples were examined using a UV-Visible spectrometer (OCEAN-HDX-XR). FTIR data were recorded to study the molecular vibration. Raman analysis of the ZnO thin film samples was carried out in a confocal Raman microscope (Alpha 300RA, WITec).

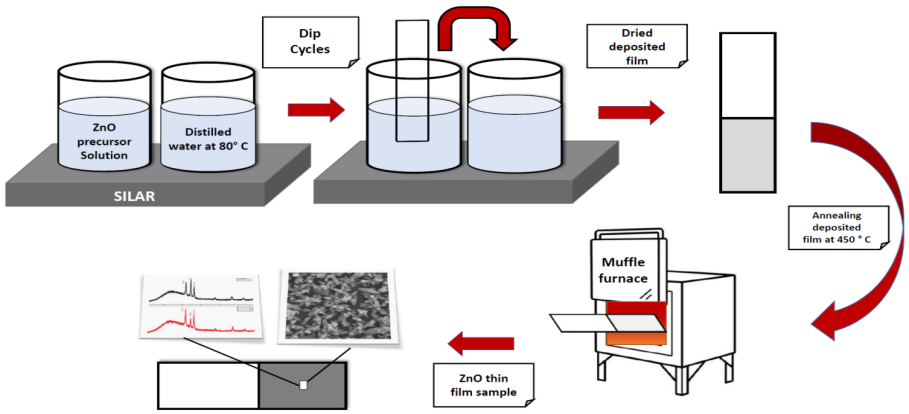

Fig. 1. Schematic representation of ZnO film deposition process.

3. Result and discussion

3.1. Structural analysis

The XRD diffractions at different angles for samples S1 and S2 are represented in Fig 2. For both samples, mainly (100),(002), and (101) peaks were identified. These peaks were identified by comparing the 2θ value with standard JCPDS data[38]. For samples S1 and S2, these were found to exist at 31.77^0, 34.47^0, 36.268^0 and 31.793^0, 34.452^0, 36.243^0 respectively. Both the samples are observed to be crystalline in nature, where in sample S1 the intensities of the peaks were comparable to one another indicating homogenous growth in all directions with the formation of small-size crystallites leading to polycrystalline thin film due to the precursor medium. In sample S2 maximum intensity was observed for (100) peak giving an inference of film growth spread along a surface substrate[39].

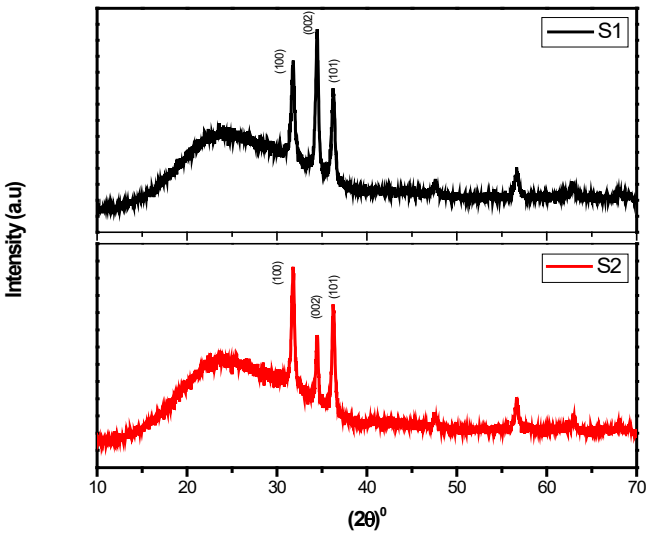

Fig. 2. XRD spectra of ZnO thin film samples S1 and S2.

From the obtained θ values and FWHM (β) values crystallite size along the maximum intensity plane was calculated using Scherrer's formula,

$$D = \frac{0.9\lambda}{\beta Cos\Theta_{\beta}} \quad (1)$$

where λ was the wavelength of the X-ray, β is the FWHM value, and θ_{β} is the diffraction angle. As predicted from the intensities of peaks the small value of crystallite size was obtained for samples S1 and S2. Calculated values are shown in Table 1.

Table 1. 2Ɵ, FWHM and Crystallite size of samples S1 and S2.

Sample	2Ɵ	FWHM (β^0)	Crystallite size D (nm)
S1	34. 470	0.365	22.789
S2	31.793	0.360	22.945

From Bragg's law, lattice constants 'a' and 'c' for the ZnO wurtzite structure can be calculated using

$$a = \frac{\lambda}{\sqrt{3}Sin\theta} \text{ and } c = a = \frac{\lambda}{Sin\theta} \quad (2)$$

From obtained 'a', 'c' values volume of the cell could be determined as

$$V = 0.866 \times a^2 \times c. \quad (3)$$

In cells, Zn-O bond lengths were identified as,

$$L = \sqrt{\left(\frac{a^2}{3} + (\frac{1}{2} - u)^2 c^2\right)} \quad (4)$$

where positional parameter,

$$u = \frac{a^2}{3c^2} + 0.25 \quad (5)$$

which is a measure of Oxygen ion displacement. Thus, obtained values are given in Table 2, out of which 'a' and 'c' values confirm the hexagonal wurtzite structure of ZnO samples. The theoretical value of c/a and 'u' were 1.633 and 0.375 for ZnO.

Table 2. Lattice parameters, atomic packing factor, cell volume, positional parameter, and bond length of samples S1 and S2.

Sample	Lattice parameters (A^0) a	c	Atomic packing factor (c/a)	Volume V $(A^0)^3$	Positional parameter u	Bond length L(Zn-O) (A^0)
S1	3.2446	5.1996	1.6025	47.4034	0.3797	1.9747
S2	3.2433	5.202	1.6039	47.3873	0.3795	1.9745

The measure of defects inside a crystal could be identified with a quantity called dislocation density δ which is identified as $\delta = \frac{1}{D^2}$. The intrinsic strain during the clustering of crystal gives the parameter micro strain Ɛ. The specific surface area of the films could be calculated as $A= \frac{6}{D\times\rho}$, where D is the average particle size(nm), ρ is the density of ZnO (5.606g/cm^3). All these calculated parameters were given in Table 3. Sample with fewer defects and Micro strain and with a more specific surface area is preferable mainly for optoelectronic and sensor applications. Stress is calculated using the formula

$$\sigma = -453.6\times10^9\left(\frac{C-C_0}{C_0}\right) \quad (6)$$

where C is the lattice parameter of the sample and C_0 is strain free lattice constant of ZnO and it is 5.2066A^0. The obtained values are given in Table 3.

Table 3. Dislocation density, strain, specific surface area, and residual stress of samples S1 and S2.

Sample	Dislocation density $\delta\times10^{-3}(A^0)^{-2}\times10^{-5}$	Strain Ɛ (rad) $\times10^{-3}$	Specific surface area $A\times10^4 m^2/kg$	Residual stress $\sigma\times10^9$ (N/m^2)
S1	1.9254	5.133	4.3758	0.6098
S2	1.8993	5.515	4.6646	0.4007

Out of the calculations, it is observable that sample S2 is available with fewer dislocations, more specific surface area, and less residual stress.

3.2. Surface analysis

The difference in precursor medium leads to a difference in the morphology of ZnO thin film samples as shown in the FESEM images of samples S1 and S2 in Fig 3. Both films were observable without cracks or other defects with high-quality nanorod formation. The majority of the nano-rods in sample S1 had their nuclei on one another in contrast to the development from the substrate. The lengths and forms of the nanorods in sample S1 are erratic and non-uniform. These formations may be due to different conditions like the PH of chemicals, the charge distribution in the medium, etc[40]. The large nano particle causes a decrease in interfacial area and hence less tensile strength. This may lead to deterioration in the performance of the sample.

Nanoparticle growth on sample S2 was identified to be highly oriented without stacking or dislocation defects in the sample and the vertical alignment and grain boundary perfection are exceptional. Clusters of particles indicating their growth from spontaneous nucleation. The existences of the individual road-like particle's growth inside clusters are visible in close observation of the image. Intimation of flower-like micro-clustered morphology was observed to be spread over the surface of S2. Generally, these types of morphology contribute to improved charge transportation in films [41]and hence are observed to be a selectable material for engineering applications.

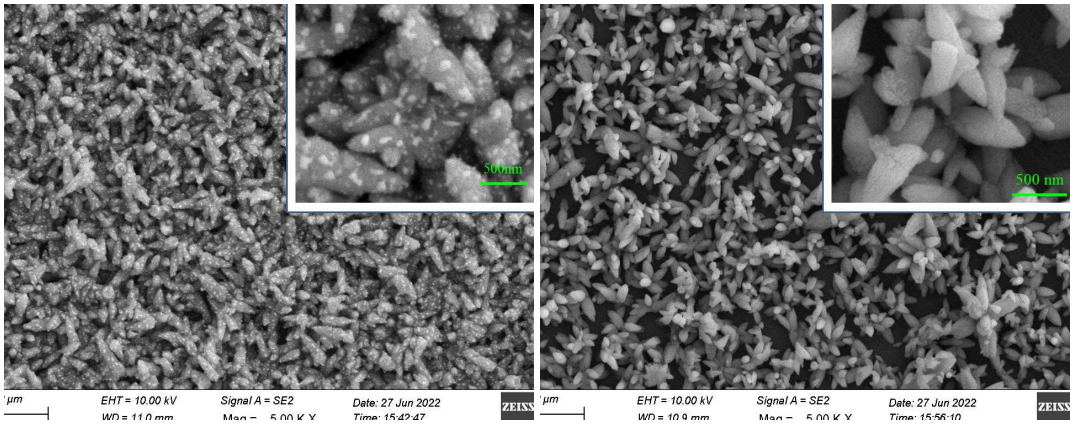

Fig. 3. FESEM images of ZnO thin film samples S1 and S2.

3.3. Electrical analysis

The Four-point probe method is used to analyze the electrical properties of manufactured ZnO thin films to determine how they may affect optoelectronic devices. Voltage (V) is measured across the inner probes for the ZnO thin film with thickness 't' by injecting current (I) through the outer probes.

The electrical resistivity (ρ) was determined by measuring the probes' consistent spacing (s).[42]

$$\rho = 4.532\left(\frac{V}{I}\right)t = R_s t \tag{7}$$

where 'R_s' is the sheet resistance. The measured values of resistivity of samples S1 and S2 are reported in Table 4.

Table 4. Sheet resistance of samples S1 and S2.

Sample	**Sheet resistance $R_s \times 10^6$ (Ω/□)**
S1	49.99
S2	49.83

3.4. Optical analysis

The electronic transition of the prepared samples S1 and S2 were analyzed with optical absorption spectra. Over the visible range, the transmittance of sample S2 was found to be more than that of S1 from Fig 4(a). This may be due to the higher removal of the $Zn(OH)_2$ phase during annealing which might have led to the structural homogeneity of sample S2[43]. The better transmittance observed for sample S2 may be due to large grain size and higher crystalline size which were evident respectively from SEM and XRD images. Fig 4(b) shows the absorbance of the samples, from which it could be identified that both samples show low absorbance over the visible range which is a general ZnO characteristic[44]. Almost over this range, the absorbance of sample S1 was found to be more than that of S2. Peaks were visible in samples S1 and S2 respectively at 367.21nm and 369.45nm, which may be characteristic ZnO band gap for pure ZnO samples. Comparing it with a bulk ZnO value of 373nm, peaks in samples were observed to be blue shifted indicating strain effect, whereas the slight red shift observable in the peak of the sample was evidence of an increase in its particle size[45].

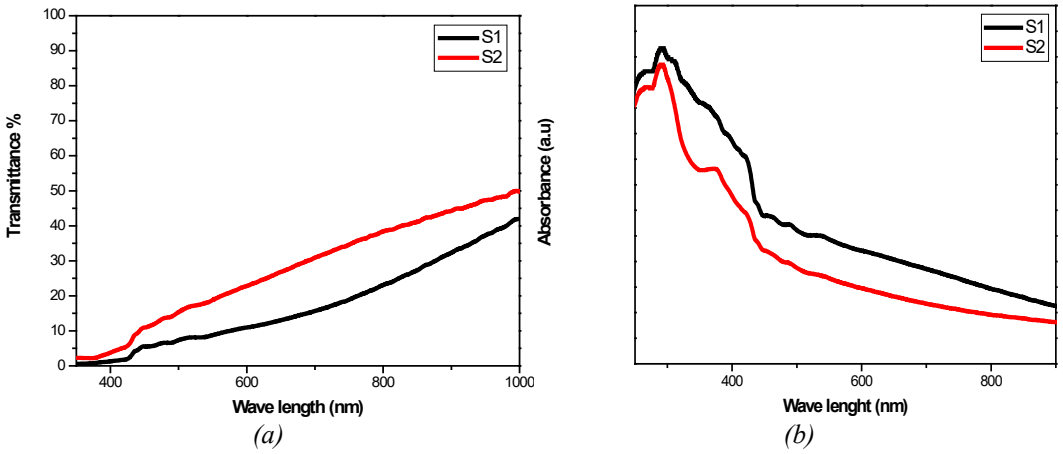

Fig. 4. Optical spectra of ZnO thin film samples S1 and S2(a) Transmittance, (b) Absorbance.

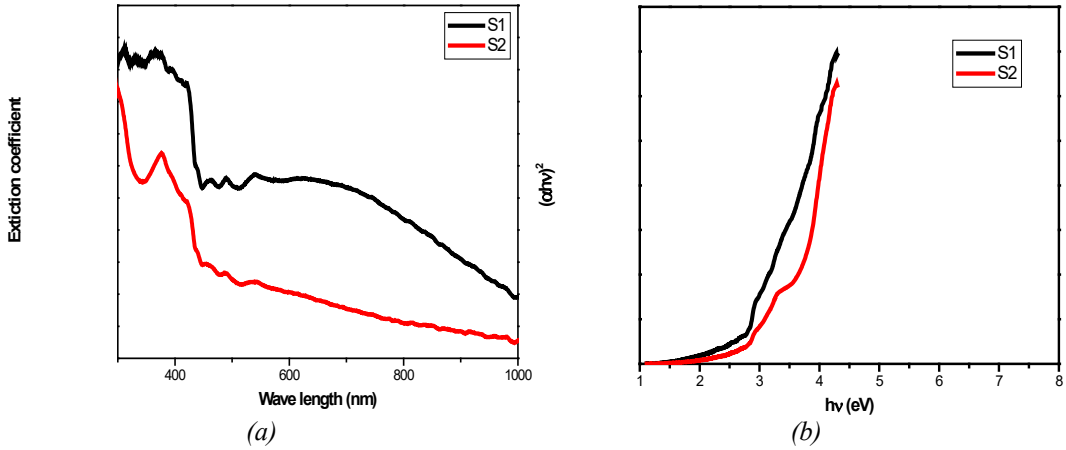

Fig. 5. (a) Extinction coefficient Vs Wavelength and (b) Tauc plot for samples S1 and S2.

The extinction coefficient (k) variation with wavelength was represented in Fig 5(a) from which reduced values of 'k' for the curve of sample S2 were found. Another way this could be considered as a measure of defects is since the density of structural defects is proportional to the lack of crystallinity of the sample[46]. For an improved crystallinity of the sample, defects will be reduced resulting in low optical absorption. Hence extinction coefficient variation underlines the better crystallinity and presence of lesser defects in sample S2[47].

Optical band gap energy 'E_g' and absorption coefficient 'α' are related as $(\alpha h\nu)^n = K(h\nu - E_g)$, where 'hν' is incident photon energy, K is energy dependent constant, and n = 2for direct band gap material. The plot of $(\alpha h\nu)^2$ Vs photon energy of the samples with the linear fit about the absorption edges shows the quality of samples synthesized, which were shown in Fig 5(b). Over a wide range of photons, energy variations were observed to be linear indicating a direct transition. A red shift of absorption edges was observed from sample S1 to sample S2. The shift was observed from 3.052 eV to 3.365eV. The lower value of the absorption edge observed for sample S1 may be attributed to the presence of defects in the sample[48].

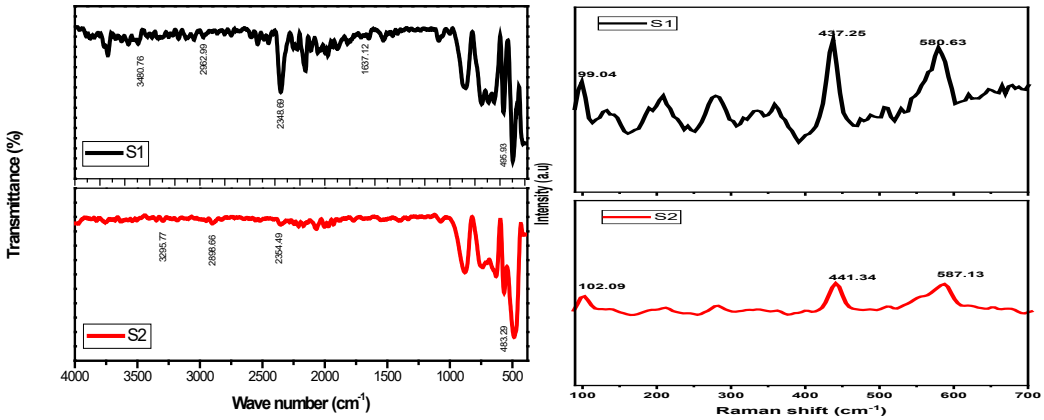

Fig. 6. (a) FTIR spectra and (b) Raman spectra of samples S1 and S2.

The vibrational properties of the prepared samples were investigated with FTIR spectroscopy and presented in Fig 6(a). FTIR spectra of prepared samples S1 and S2 between wave number range 380-4000cm^{-1}are illustrated in the figure. Absorption bands were observed at 495.93cm^{-1} and 483.29 cm^{-1} respectively for samples S1 and S2. These values indicate Zn-O stretching vibrations of the samples. The absorption curve at 1637.12 cm^{-1} represents the H_2O vibration band which may be due to the absorption of water from the atmosphere on the surface of sample S1. The presence of absorbed CO_2 molecules on the surface of samples S1 and S2 are revealed by the bands at 2348.69 cm^{-1}and 2354.49 cm^{-1} respectively. At 2962.99 cm^{-1} and 2898.66 cm^{-1}, respectively on S1 and S2 bands are observed, which might have emerged due to C-H stretching vibration in the alkane group. O-H symmetric stretching vibration of samples S1 and S2 is evident from bands at 3480.76 cm^{-1} and 3295.77 cm^{-1} respectively[49].

ZnO thin films forma wurtzite crystal structure and group theory predicts the potential optical modes as

$A_1(TO)+ 1A_1(LO)+ 2B_1+ 1E_1(TO) + 1E_1(LO)+2E_2$. In which two B_1 modes are not Raman active. (LO) and (TO) identifies the longitudinal and transverse optical components, since A_1 and E_1 modes are infrared active too. The Raman spectra of the ZnO thin film samples S_1 and S_2 are shown in Fig 6(b). The phonon frequencies identified from the spectra of sample S1 are: E_2(high)= 437.25 cm^{-1}, E_2(low)= 99.04 cm^{-1}, E_1(LO)= 580.63 cm^{-1}, and the same peaks identified for sample S2 are respectively at 441.34 cm^{-1}, 102.09 cm^{-1} and 587.13 cm^{-1}. E_2 vibration mode is characteristic of wurtzite crystal structure. E_1(LO) mode is the identification of defect formations such as free carrier lack, interstitial Zn, oxygen absence, etc. The weak intensity of this peak for sample S2suggests the presence of a low density of defects in this sample. $1E_1$(TO) mode of samples is very weak to be identified, which could be interpreted due to the low value of stress developed in samples. E_2 phonon frequency is an identification residual stress in ZnO thin film samples. An increased value of phonon frequency identified for sample S_1 is evidence of the compressive stress present in the sample, which might have arisen due to a mismatch of thermal expansion coefficients sample material and glass substrate. The sharpness of the E_2 peak is the indicator of grain size of the samples and it could be concluded that sampleS2is available with more grain size[50].

3.5. Solar cell modeling

Using a finite difference drift-diffusion model, trapping and de-trapping are found in this simulation of carrier transport. The bi-polar drift-diffusion equations are solved for electrons and holes. Hole current flux density is designated as ‘Jp’, while electron current flux density is abbreviated as ‘Jn’.

$$J_n = q\mu_e n_f \frac{\partial E_{LUMO}}{\partial x} + qD_n \frac{\partial n_f}{\partial x} \quad (8)$$

$$J_p = q\mu_h p_f \frac{\partial E_{HOMO}}{\partial x} - qD_p \frac{\partial p_f}{\partial x} \quad (9)$$

Here, 'q' stands for the charge of an electron, 'μ_e' and 'μ_h'stand for electron and hole mobility, and 'D_n', 'D_p' stands for the electron and hole diffusion coefficients.

To determine the device's built-in potential distribution, 'ϕ' is identified from Poisson's equation.

$$\frac{d}{dx}.\varepsilon_0\varepsilon_{0r}\frac{d\phi}{dx} = q(n_f + n_t - p_f - p_t - N_{ad}) \quad (10)$$

where ε_0 and ε_r are permittivities of respectively air and active medium. 'n_f' is free electron density and 'n_t' is trapped electron density, 'p_f' is free hole density, and 'p_t' is trapped hole density. 'N_{ad}' is the doping density[51].

The default values of density of states of Perovskite and PEDOT: PSS layers, available in the simulator were adopted for modeling, whereas experimentally extracted values and values from the literature review were input for the ZnO electron transport layer.

The percentage of the fill factor can be found as

$$FF = \frac{V_{max} \times I_{max}}{V_{oc} \times I_{sc}} \quad (11)$$

The power conversion efficiency of the Solar cell is the ratio of power output (P_{out}) to that of power input (P_{in}) and which could be calculated as,

$$\eta = \frac{V_{oc} \times J_{sc} \times FF}{P_{in}} \quad (12)$$

3.5.1. Pervoskite solar cell

One of the most commonly used perovskite structures for Solar cell application is Methylammonium lead iodide ($CH_3NH_3PbI_3$) perovskite. This material shows a strong dependence on crystalline nature over a wide range of temperatures. Because $CH_3NH_3PbI_3$ has high carrier mobility, electrons, and holes can move through it quickly and effectively. Recombination losses—where the charge carriers recombine before creating a current—are decreased as a result. Furthermore, $CH_3NH_3PbI_3$ is capable of efficiently absorbing sunlight and generating electrical energy due to its appropriate band gap and energy levels[52]. Perovskite Solar cells are a good choice for large-scale solar power systems due to the inexpensive cost of the components necessary to create them. Due to the unique composition and electrical characteristics of perovskites, perovskite Solar cells have shown tremendous promise for high carrier mobility. Due to its unique composition and electrical characteristics and broad-spectrum light absorption, power conversion efficiencies of perovskite solar cells are in leap over this decade, reporting a maximum value of 26.1% according to the current National Renewable Energy Laboratory (NREL) solar cell efficiency chart.

The device architectures possible could be by stacking the layer in order as Substrate / ITO/PEDOT: PSS/Perovskite/ZnO/Ag, which will form the conventional p-i-n Perovskite Solar cell. Perovskite is the active layer in which charge carriers are generated. ZnO is the ETL and PEDOT: PSS is the HTL which are also fixed as 'active layers' in the simulator. 'ITO' and 'Ag' are selected as contact layers. In this case, illumination is happening through the ITO layer and electron-hole pairs will be generated in the Perovskite layer, which will get transferred to respective electrodes via ETL and HTL. The conventional Perovskite solar layer arrangement is shown in Fig 7. The default values available for the active layer and HTL were 400nm and 200nm respectively in the simulator.

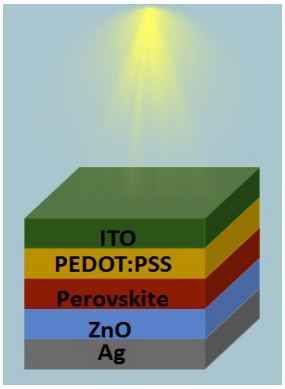

Fig. 7. Layer arrangements of perovskite solar cell.

3.5.2. Effect of variation of Perovskite layer thickness on the performance of the solar cell

The variations of J_{sc} values with the thickness of the Perovskite layerfor devices fabricated with samples S1 and S2 are plotted in Fig 8(a). Both curves show a similar tendency of variations with slightly different values. It is noted that as the film thickness increases, it can absorb more incident light, leading to an increase in the number of generated electron-hole pairs. As a result, Jsc increases. However, if the absorber layer thickens, it can cause more charge carriers (such electrons and holes) to recombine inside the material before they reach the electrodes. With growing thickness, this recombination effect intensifies, resulting in a decline in Jsc.More over beyond a given thickness, the increase in light absorption brought on by more material may saturate because the depth of light penetration is constrained, which causes Jsc to decrease. Hence the over all tendcy of this curve leads into a bell shape. In direct comparison, the device with sample S2 exhibits a higher value of conductivity, resulting in a marginally higher value of J_{sc} than the device with sample S2. It might be obtained due to the fact that, in experimentally prepared samples S1 and S2, sample S2 was available with fewer defects. Fig 8(b) shows the V_{oc} curve with thickness of the Perovskite layer. For both devices with samples S1 and S2, the V_{oc} shows a general increasing trend up to 500nm , which might have been attributed to a decrease in the recombination of charge carriers. The increase in series resistance caused by the layer's decrease in carrier concentration and carrier mobility can be used to describe the general trend of FF decrement with Perovskite layerthickness increase, which is presented in Fig 8(c). PCE values were obtained at a layer thickness of 500nm for both samples and the values are respectively 18.5% and 18.65%. The efficiency parameter variations with Perovskite layer thickness are shown in Fig 8(d)

3.5.3. Effect of variation of HTL layer thickness on the performance of the solar cell

Variation of electrical parameters with the HTL layer thickness for the Solar cells fabricated with Sample S1 and Sample S2 is identified.

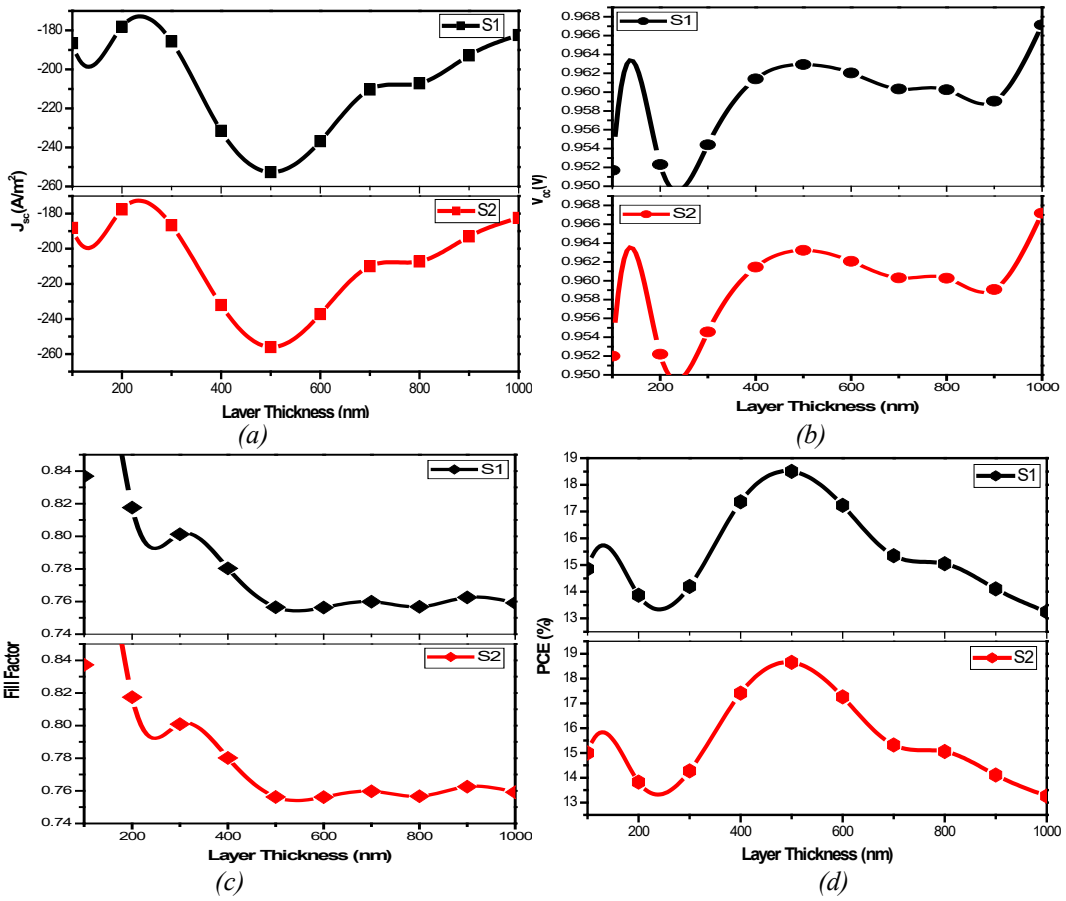

Fig. 8. Variation of electrical parameters a) Jsc, b) Voc, c) FF, and d) PCE with the Perovskite layer thickness for the Solar cells fabricated with Sample S1 and Sample S2.

The maximum efficiency obtained for Solar cells fabricated with Samples S1 and S2 are respectively 21.88% and 21.96% for an HTL layer thickness of 100nm. For this thickness, the J_{sc}, V_{oc}, and FF respectively obtained as -299.848 A/m^2, 0.9666 V, 0.7548 for sample S1 and -300.990 A/m^2, 0.9667 V, 0.7546 for sample S2. When HTL thickness is <100nm, there may be chances that due to the surface recombination happening at HTL and contact layer interface leaden to a decrease in efficiency. The variation of Fill factor values with the HTL thickness gives an indication of changes happening in series resistance. As the HTL thickness increased from 50-100nm, the efficiency of the cell increases from almost 15- 22% with a change of fill factor from 0.775-0.754 for both devices using samples S1 and S2. The reduction in fill factor with the increase in HTL thickness may be considered due to the series resistance offered by the HTL[53]. Further, an increase in HTL thickness up to 500nm resulted in a reduction of efficiency of almost 10%.

Maximum efficiency of the Solar cell was identified for an HTL thickness of 100nm, a Perovskite layer thickness of 400nm with ZnO ETL thickness of obtained samples. The electrical parameters variations with Perovskite layer thickness are shown in Fig 9(a),(b),(c),(d). The input parameters used for simulating the Solar cell are reported in Table 5.

Table 5. Input parameters for numerical simulation for optimum values.

Input parameters	PEDOT: PSS	Perovskite	ZnO
Thickness (nm)	100	400	996 (S1), 1015 (S2)
Relative permittivity ε_r	3	20	20
Optical band gap E_g (eV)	1.6	1	3.052(S1), 3.365 (S2)
Electron affinity (eV)	-5.2	-3	-4.3
Electron mobility (m^2/V.s)	0.002	0.002	0.02
Hole mobility (m^2/V.s)	0.002	0.002	0.018
Electron density of states (m^{-3})	5×10^{25}	1×10^{26}	5×10^{25}
Hole density of states (m^{-3})	5×10^{25}	1×10^{26}	5×10^{25}
Thermal conductivity(W $m^{-1}C^{-1}$)	2.2	1	50
Electron relaxation time (s)	1	1×10^{-8}	1×10^{-12}
Hole relaxation time (s)	1	1×10^{-9}	1×10^{-12}

The corresponding electrical parameters are listed in a table and the J-V plot is presented in Fig. 10.

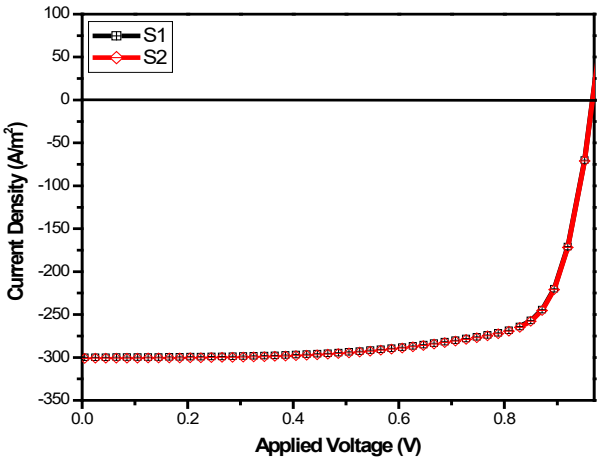

Fig. 10. J-V Curves of perovskite solar cells with samples S1 and S2.

Fig 10 shows the current density (J_{sc}) vs Voltage (V) for the devices simulated with samples S1 and S2as ETL. The open circuit voltage (V_{oc}), short circuit current (J_{sc}), fill factor (FF), and power conversion efficiency (PCE) for a device with sample S1 are recorded as 0.9666V, -299.84 A/m^2, 0.7548, and 21.88% respectively. For the device with sample S2, the values obtained for these parameters are 0.9667V, -300.99 A/m^2, 0.7546, and 21.96 %. The obtained values indicate the efficient performance of the device fabricated with sample S2 over the other device. The PCE values obtained for the devices are observed to be consistent with the J_{Sc} values indicating that the medium of preparation of ZnO thin films influences Solar cell performance. Solar cell parameters obtained for devices with samples S1 and S2 are reported in Table 6.

Table 6. Solar cell parameters of the devices with samples S1 and S2.

Solar cell with ZnO sample	V_{oc} (V)	J_{sc} (A/m^2)	FF	PCE (%)
S1	0.9666	-299.84	0.7548	21.88
S2	0.9667	-300.99	0.7546	21.96

The obtained values of recombination constant, electron mobility at $P_{max,}$ and Average mobility at J_{sc} are reported in table 7. It is observable that the device with sample S2 is provided with better values than that of the device with sample S1.

Table 7. Recombination constant at V_{oc}, electron mobility at $P_{max,}$ and average mobility at J_{sc} of the devices with samples S1 and S2.

Solar cell with ZnO sample	**Total carriers at $V_{oc}\times10^{23}$**	**Recombination rate at V_{oc} ($m^{-3}s^{-1}$) $\times10^{27}$**	**Electron mobility at $P_{max}\times10^{-2}$($m^2V^{-1}s^{-1}$)**	**Average mobility as $J_{SC}\times10^{-2}$ ($m^2V^{-1}s^{-1}$)**
S1	1.1549	1.3070	1.3676	1.3035
S2	1.1549	1.3123	1.3676	1.3038

Absorbed Photon density for devices with samples S1 and S2 with normalized photon absorbed per layer of Solar cells are shown in Fig 11(a)&(b), and Fig 12(a)&(b) respectively. It is evident from the figures that the photon absorption is maximum between 200 to 600nm, where the absorber layer is placed in the devices. A slight improvement in photons absorbed is shown by the device with sample S2 in this region.

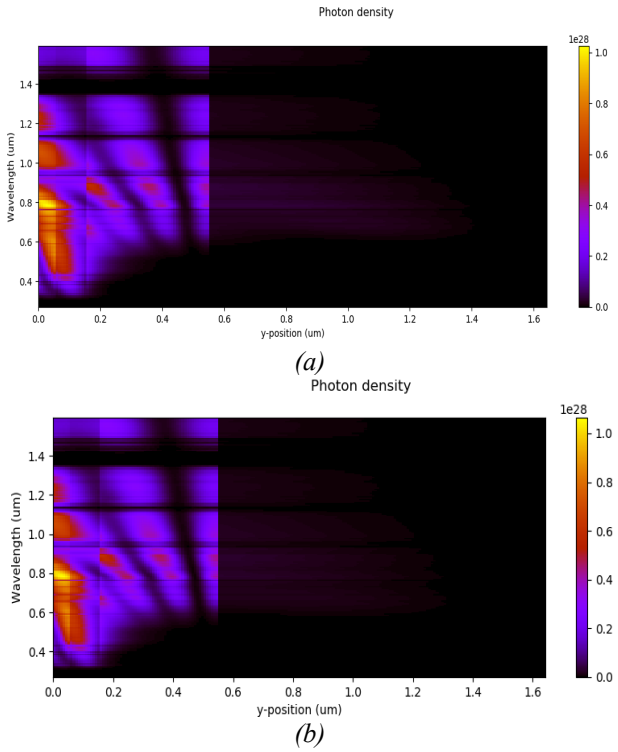

Fig. 11. Absorption photon spectra with the layer thickness for devices fabricated with samples a) S1 and b) S2.

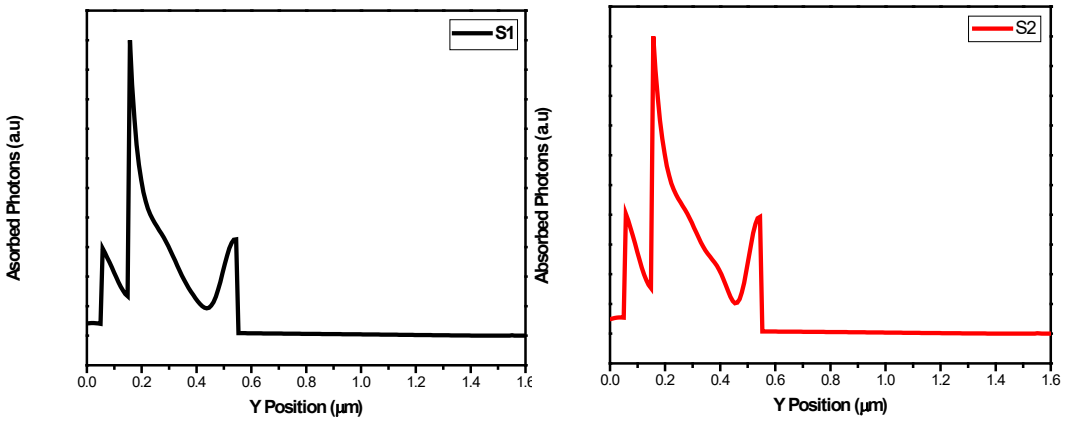

Fig. 12. Normalized photons absorbed with the layer thickness for devices fabricated with samples a) S1 and b) S2.

External quantum efficiency (EQE) is the ratio of the number of charge carriers generated by photon illumination to the number of incident photons. It is calculated as the product of four efficiencies: charge collection (CC), charge separation (CS), Exciton dissociation (ED), and Absorption (A), which is given as $EQE(\lambda) = \eta_{CC}(\lambda) \times \eta_{CS}(\lambda) \times \eta_{ED}(\lambda) \times \eta_{A}(\lambda)$ [54]**.** Fig 13 shows the variation of EQE with wavelength and a general trend of decreasing from a maximum EQE value for respective samples were observed in the wavelength ranges of 280 – 1600nm. An improvement in the spectrum was observed for OSC with sample S2 for most of the wavelength range, which is also evident from UV-visible absorption spectra. The improved EQE may be related directly to the enhanced contact supplied by ZnO nanorods of sample S2, leading to reduced resistance and offering high-charge transport through the ETL layer. The higher values of J_{sc} and FF of OSC with sample S2 support this fact.

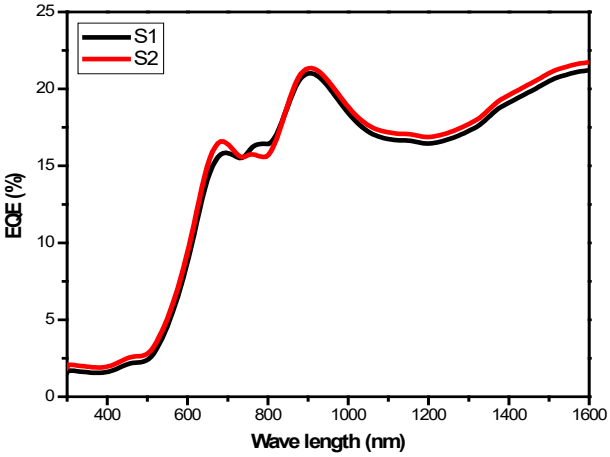

Fig. 13. EQE Curve of Perovskite Solar cells with samples S1 and S2.

4. Conclusion

In summary, high-quality ZnO thin films from Zinc Acetate and Zinc Chloride precursor media were deposited on a glass substrate using the SILAR method and named samples S1 and S2 respectively. ZnO thin films deposited from both precursors are showing high crystalline nature, whereas sample S2 is available with fewer dislocations, a more specific surface, and less residual

stress. Both samples identified with nanorod structure morphology while sample S2's surface is covered with nanorods with a perfect grain boundary. Electrical conductivity measurements revealed a low value of sheet resistance of sample S2. Sample S2 demonstrated higher transparency in the visible range and optical band gap energy with high purity is proven from FTIR and Raman studies. For the numerical modeling of the Perovskite Solar cell, the active layer thickness and HTL thickness were optimized as 400nm and 100 nm respectively. Numerical modeling of Perovskite Solar cells with the prepared samples contributed to the high value of 'J_{sc}' and 'PCE' for the device fabricated with sample S2 as the electron transport layer. The efficiency of the device obtained was 21.96%. Thereby, we are concluding that by using Zinc Chloride precursor in the SILAR method, high-quality ZnO thin films can be prepared, which are beneficial in applications such as the electron transport layer in Perovskite Solar cells.

Acknowledgments

The authors acknowledge the UV-Visible instrumentation facility established under DST-SERB sponsored research project for Core Research Grant (CRG/2019/006624).

References

[1] Malik G, Mourya S, Jaiswal J, Chandra R. Materials Science in Semiconductor Processing 2019 Sep 1;100:200-13; https://doi.org/10.1016/j.mssp.2019.04.032

[2] Rohith NM, Kathirvel P, Saravanakumar S, Mohan L., Optik. 2018 Nov 1;172:940-52; https://doi.org/10.1016/j.ijleo.2018.07.045

[3] Li Y, Shan LX, Wang RC, Lian XX, Zhou QJ., Ceramics International. 2022 Aug 1;48(15):22467-75; https://doi.org/10.1016/j.ceramint.2022.04.256

[4] Sharma SC., Optik. 2016 Aug 1;127(16):6498-512; https://doi.org/10.1016/j.ijleo.2016.04.036

[5] Kumar N, Srivastava A., Journal of Alloys and Compounds. 2018 Feb 25;735:312-8; https://doi.org/10.1016/j.jallcom.2017.11.024

[6] Khudiar SS, Mutlak FA, Nayef UM., Optik. 2021 Dec 1;247:167903; https://doi.org/10.1016/j.ijleo.2021.167903

[7] Rotella H, Mazel Y, Brochen S, Valla A, Pautrat A, Licitra C, Rochat N, Sabbione C, Rodriguez G, Nolot E., Journal of Physics D: Applied Physics. 2017 Nov 7;50(48):485106; https://doi.org/10.1088/1361-6463/aa920b

[8] Kumar KD, Valanarasu S, Kathalingam A, Ganesh V, Shkir M, AlFaify S., Applied Physics A. 2017 Dec;123:1-1; https://doi.org/10.1007/s00339-017-1426-z

[9] Sahoo B, Pradhan SK, Mishra DK, Sahoo SK, Nayak RR, Behera D., Optik. 2021 Feb 1;228:166134; https://doi.org/10.1016/j.ijleo.2020.166134

[10]Pathan HM, Lokhande CD., Bulletin of Materials Science. 2004 Apr;27:85-111; https://doi.org/10.1007/BF02708491

[11] Fairose S, Ernest S., Physica B: Condensed Matter. 2019 Mar 15;557:63-73; https://doi.org/10.1016/j.physb.2018.12.041

[12] Gao XD, Li XM, Yu WD., Applied Surface Science. 2004 May 15;229(1-4):275-81; https://doi.org/10.1016/j.apsusc.2004.02.004

[13] Vargas-Hernandez C, Jimenez-Garcia FN, Jurado JF, Granada VH., Microelectronics Journal. 2008 Nov 1;39(11):1349-50; https://doi.org/10.1016/j.mejo.2008.01.056

[14] Belkhalfa H, Ayed H, Hafdallah A, Aida MS, Ighil RT., Optik. 2016 Feb 1;127(4):2336-40; https://doi.org/10.1016/j.ijleo.2015.11.126

[15] Ghos BC, Farhad SF, Patwary MA, Majumder S, Hossain MA, Tanvir NI, Rahman MA, Tanaka T, Guo Q., ACS omega. 2021 Jan 21;6(4):2665-74; https://doi.org/10.1021/acsomega.0c04837

[16] Yergaliuly G, Soltabayev B, Kalybekkyzy S, Bakenov Z, Mentbayeva A., Scientific reports. 2022 Jan 17;12(1):1-3; https://doi.org/10.1038/s41598-022-04782-2

[17] Djurišić AB, Liu FZ, Tam HW, Wong M, Ng A, Surya C, Chen W, He ZB., Progress in Quantum Electronics. 2017 May 1;53:1-37; https://doi.org/10.1016/j.pquantelec.2017.05.002

[18] Song TB, Chen Q, Zhou H, Jiang C, Wang HH, Yang YM, Liu Y, You J, Yang Y., Journal of Materials Chemistry A. 2015;3(17):9032-50; https://doi.org/10.1039/C4TA05246C

[19] Kim JY, Lee JW, Jung HS, Shin H, Park NG., Chemical Reviews. 2020 Jul 28;120(15):7867-918; https://doi.org/10.1021/acs.chemrev.0c00107

[20] Karimi E, Ghorashi SM., Optik. 2017 Feb 1;130:650-8; https://doi.org/10.1016/j.ijleo.2016.10.122

[21] Kumar NS, Naidu KC., Journal of Materiomics. 2021 Sep 1;7(5):940-56; https://doi.org/10.1016/j.jmat.2021.04.002

[22] Jacobsson TJ, Correa-Baena JP, Halvani Anaraki E, Philippe B, Stranks SD, Bouduban ME, Tress W, Schenk K, Teuscher J, Moser JE, Rensmo H., Journal of the American Chemical Society. 2016 Aug 17;138(32):10331-43; https://doi.org/10.1021/jacs.6b06320

[23] Wang S, Dong W, Fang X, Zhang Q, Zhou S, Deng Z, Tao R, Shao J, Xia R, Song C, Hu L., Nanoscale. 2016;8(12):6600-8; https://doi.org/10.1039/C5NR08344C

[24] Zhang G, Zheng Y, Shi Y, Ma X, Sun M, Li T, Yang B, Shao Y., ACS Applied Materials & Interfaces. 2022 Feb 22;14(9):11500-8; https://doi.org/10.1021/acsami.1c24349

[25] Izadi F, Ghobadi A, Gharaati A, Minbashi M, Hajjiah A., Optik. 2021 Feb 1;227:166061; https://doi.org/10.1016/j.ijleo.2020.166061

[26]Tseng ZL, Chiang CH, Wu CG., Scientific reports. 2015 Sep 28;5(1):13211; https://doi.org/10.1038/srep13211

[27] Song J, Bian J, Zheng E, Wang XF, Tian W, Miyasaka T., Chemistry Letters. 2015 May 5;44(5):610-2; https://doi.org/10.1246/cl.150056

[28] Nair S, Patel SB, Gohel JV., Materials Today Energy. 2020 Sep 1;17:100449; https://doi.org/10.1016/j.mtener.2020.100449

[29] Lin L, Jones TW, Yang TC, Duffy NW, Li J, Zhao L, Chi B, Wang X, Wilson GJ., Advanced Functional Materials. 2021 Jan;31(5):2008300; https://doi.org/10.1002/adfm.202008300

[30] Shafi MA, Khan L, Ullah S, Shafi MY, Bouich A, Ullah H, Mari B., Optik. 2022 Mar 1;253:168568; https://doi.org/10.1016/j.ijleo.2022.168568

[31]Gahtar A, Rahal A, Benhaoua B, Benramache S., Optik. 2014 Jul 1;125(14):3674-8; https://doi.org/10.1016/j.ijleo.2014.01.078

[32] Alsaad AM, Ahmad AA, Qattan IA, Al-Bataineh QM, Albataineh Z., Crystals, 2020 Mar 27;10(4):252; https://doi.org/10.3390/cryst10040252

[33] Theerthagiri J, Salla S, Senthil RA, Nithyadharseni P, Madankumar A, Arunachalam P, Maiyalagan T, Kim HS., Nanotechnology 2019 Jul 11;30(39):392001; https://doi.org/10.1088/1361-6528/ab268a

[34]Sims L, Hörmann U, Hanfland R, MacKenzie RC, Kogler FR, Steim R, Brütting W, Schilinsky P., Organic Electronics. 2014 Nov 1;15(11):2862-7; https://doi.org/10.1016/j.orgel.2014.08.010

[35] Abdallaoui M, Sengouga N, Chala A, Meftah AF, Meftah AM., Optical Materials. 2020 Jul 1;105:109916; https://doi.org/10.1016/j.optmat.2020.109916

[36] Sreedev P, Sreekumar G, Samad AA, Rakhesh V, Roshima NS., AIP Conference Proceedings 2021 Sep 13 (Vol. 2369, No. 1). AIP Publishing; https://doi.org/10.1063/5.0062635

[37] Manoj M, Padmanabhan S, Vamadevan R, Sujatha RN, Shankar B., AIP Conference Proceedings 2020 Nov 9 (Vol. 2287, No. 1). AIP Publishing; https://doi.org/10.1063/5.0030050

[38] Shatnawi M, Alsmadi AM, Bsoul I, Salameh B, Mathai M, Alnawashi G, Alzoubi GM, Al-Dweri F, Bawa'aneh MS., Results in Physics. 2016 Jan 1;6:1064-71; https://doi.org/10.1016/j.rinp.2016.11.041

[39]Bao D, Gu H, Kuang A., Thin solid films. 1998 Jan 14;312(1-2):37-9; https://doi.org/10.1016/S0040-6090(97)00302-7

[40]Baruah S, Dutta, Journal of Crystal Growth. 2009 Apr 1;311(8):2549-54; https://doi.org/10.1016/j.jcrysgro.2009.01.135

[41] Meng Y, Lin Y, Lin Y., Ceramics International. 2014 Jan 1;40(1):1693-8; https://doi.org/10.1016/j.ceramint.2013.07.065

[42] Kumar S, Seth R, Panwar S, Goyal KK, Kumar V, Choubey RK., Journal of Electronic Materials. 2021 Jun;50:3462-70; https://doi.org/10.1007/s11664-021-08863-2

[43]Yoon S, Huh I, Lim JH, Yoo B., Current Applied Physics. 2012 May 1;12(3):784-8; https://doi.org/10.1016/j.cap.2011.11.007

[44]López-Suárez A, Acosta D, Magaña C, Hernández F., Journal of Materials Science: Materials in Electronics. 2020 May;31:7389-97; https://doi.org/10.1007/s10854-019-02830-8

[45]Ansari AR, Hussain S, Imran M, Al-Ghamdi AA, Chandan MR., Materials Science-Poland. 2018 Jun 1;36(2):304-9; https://doi.org/10.1515/msp-2018-0041

[46]Zhang Z, Bao C, Yao W, Ma S, Zhang L, Hou S., Superlattices and Microstructures. 2011 Jun 1;49(6):644-53; https://doi.org/10.1016/j.spmi.2011.04.002

[47]Bahadur N, Srivastava AK, Kumar S, Deepa M, Nag B., Thin Solid Films. 2010 Jul 1;518(18):5257-64; https://doi.org/10.1016/j.tsf.2010.04.113

[48]Ren T, Baker HR, Poduska KM., Thin Solid Films. 2007 Jul 31;515(20-21):7976-83; https://doi.org/10.1016/j.tsf.2007.03.185

[49]Djelloul A, Aida MS, Bougdira J., Journal of Luminescence. 2010 Nov 1;130(11):2113-7; https://doi.org/10.1016/j.jlumin.2010.06.002

[50]Yahia SB, Znaidi L, Kanaev A, Petitet JP., Spectrochimica Acta Part A: Molecular and Biomolecular Spectroscopy. 2008 Dec 15;71(4):1234-8; https://doi.org/10.1016/j.saa.2008.03.032

[51]Gupta V, Srivastava A, Jain R, Sharma VK, Kumar L., Optical Materials 2022 Sep 1;131:112747; https://doi.org/10.1016/j.optmat.2022.112747

[52]Martynov YB, Nazmitdinov RG, Moià-Pol A, Gladyshev PP, Tameev AR, Vannikov AV, Pudlak M., Physical Chemistry Chemical Physics. 2017;19(30):19916-21; https://doi.org/10.1039/C7CP03892E

[53]Stolterfoht M, Wolff CM, Amir Y, Paulke A, Perdigón-Toro L, Caprioglio P, Neher D., Energy & Environmental Science. 2017;10(6):1530-9; https://doi.org/10.1039/C7EE00899F

[54]Verma AK, Agnihotri P, Patel M, Sahu S, Tiwari S., Recent Advances in Photovoltaics. 2017:299-309; https://doi.org/10.21741/9781945291371-10